nature communications

Article

https://doi.org/10.1038/s41467-025-63267-8

High-flux and anti-fouling membrane distillation membrane with VOC capture ability enabled by ZIF-8

Received: 18 February 2025

Accepted: 14 August 2025

Published online: 28 August 2025

Check for updates

Dafei Sheng[1], Xinlin Li[1], Xin Huang[1], Dou Ma[1], Chao Sun[1], Yuhao Zhu[1], Xiaoqi Wang[2], Zhipeng Wang[3], Xiao Feng[1] ✉, Shuang Zhao[1] ✉ & Bo Wang[1] ✉

Seawater desalination and wastewater purification from brackish water, shale gas extraction, and industrial processes remain vital but challenging. Membrane distillation offers a promising solution yet struggles with low flux, membrane fouling, and the permeation of volatile organic compounds alongside water vapor. Here, we introduce an omniphobic ZIF-8 composite membrane that traps volatile organic compounds under vacuum through crystal phase transitions and enhances water evaporation via linkage swing within hydrophobic micropores. This membrane, with a 92% ZIF-8 loading, fabricated through thermally induced phase separation, hot-pressing, and surface coating, can process over 38,000 L of water with 10 ppm contaminants per square meter without needing reactivation. Achieving a normalized flux of 71.8 L m^{-2} h^{-1} bar^{-1}, it outperforms conventional membranes by fivefold in treating 10.5 wt% saline water, while maintaining excellent cyclic stability over 900 h and high anti-fouling properties. This work presents an effective approach for sustainable water purification.

The pursuit of zero liquid discharge in water treatment and purification is vital for environmental sustainability, resource recovery, and water security[1–5]. However, this goal presents significant challenges, notably high salinity levels in wastewater from industrial processes, desalination plants, and mining operations, further complicated by co-existed organic pollutants[6–8]. Membrane distillation (MD) emerges as a promising solution, using hydrophobic membranes to produce freshwater under a thermal gradient at lower temperatures and pressures[9–12]. Compared to multi-effect distillation and multi-stage flash, MD offers key advantages in utilizing renewable and unconventional heat sources—such as low-grade industrial waste heat, solar thermal energy, and geothermal energy—while employing simpler, more flexible equipment[13–16]. MD also serves as an indispensable complement to reverse osmosis process, efficiently overcoming its upper salinity threshold of about 80 g L^{-1}.

Despite its potential, MD encounters two pivotal obstacles. (1) Achieving high-quality water requires the effective removal or rejection of volatile organic compounds (VOCs). However, VOCs pose a significant challenge because they can vaporize alongside water, permeating the membrane and compromising water purity. Thus, controlling VOC permeation necessitates specialized feedwater treatment and innovative membrane designs[17]. While advanced oxidation, electrochemical methods, and photocatalysis have been explored, these techniques come with limitations: continuous oxidant input or light exposure increases operational costs[18,19], and electrochemical methods carry the risk of electro-corrosion[20]. Recent efforts involve integrating functional modifiers into MD membranes to selectively reject

[1]Frontiers Science Center for High Energy Material, School of Chemistry and Chemical Engineering, Beijing Institute of Technology, Beijing, PR China. [2]PetroChina Research Institute of Petroleum Exploration & Development, Beijing, PR China. [3]State Key Laboratory of Applied Organic Chemistry, College of Chemistry and Chemical Engineering, Lanzhou Magnetic Resonance Center, Lanzhou University, Lanzhou, Gansu, PR China.
✉e-mail: fengxiao86@bit.edu.cn; shuangzhao@bit.edu.cn; bowang@bit.edu.cn

VOCs like butanol and ethyl acetate[21], but these approaches remain limited for broader VOC contaminants. While porous materials like activated carbon can adsorb VOC, they struggle to prevent desorption under MD conditions. (2) Approaches to mitigate the trade-off between vapor flux and anti-fouling or anti-wetting properties in MD membranes include surface grafting, hydrophobic or omniphobic coatings, and the incorporation of nanomaterials[22–25]. While these strategies improve fouling resistance and wetting stability, they often compromise vapor flux, challenging the balance between membrane performance and durability. Recent innovations, such as hierarchical structuring and selective functionalization, are being explored to achieve optimal flux while maintaining resistance to fouling and wetting[26]. Our recent studies have highlighted that mesopores in covalent organic framework membranes can expedite water flux via a confined evaporation enhancement effect[27].

We hypothesize that the key to tackling these obstacles involves incorporating micropores into MD membranes that facilitate VOCs entry but restrict their exit, and disrupting water molecule hydrogen bonding to boost evaporation flux. Metal-organic frameworks (MOFs) have gained considerable attention in membrane separation due to their tunable porosity, high surface area, and selective adsorption properties, making them highly promising for gas separation, nanofiltration, and desalination[28–31]. In MD, incorporating water-stable MOFs into polymer matrices via methods such as spray coating, nonsolvent-induced phase separation, and electrospinning has shown potential for enhancing flux[23,32–34]. Despite progress, VOC trapping and the trade-off between vapor flux and resistance to fouling or wetting remain largely unaddressed. Specifically, the unique "breathing" capability of several MOFs, attributed to the directional flexibility of coordination bonds allowing for reversible pore dynamics in response to external stimuli, alongside their high surface area and precise pore structure, makes them ideal for VOC trapping[35–40]. However, their crystal designs do not align with VOC molecule sizes. On the other hand, zeolitic imidazolate frameworks (ZIFs), a subclass of MOFs, feature a "swinging" effect that allows the passage of molecules larger than their defined aperture sizes[41–44]. Common VOCs in wastewater, such as toluene, chlorobenzene, and ethylbenzene, fall into the aperture and cavity dimensions of ZIF-8. Recent evidence suggests ZIF-8 undergoes a crystal structure transition under continuous external electric fields or current-driven synthesis[45–47].

In this work, inspired by these insights, we modulate the crystal phase of ZIF-8 by varying solvo-thermal synthetic conditions and uncover a mechanism whereby VOCs can trigger additional crystal phase transitions in ZIF-8 polymorphs, thereby preventing their desorption even under vacuum. A 92% ZIF-8-loading omniphobic mixmatrix membrane (MMM) is fabricated by our developed thermally induced phase separation and hot-pressing technique (TIPS-HoP)[48], demonstrating outstanding MD performance in VOC trapping, water flux, and resistance to fouling and wetting. We discover that the dynamic linker swing disrupts hydrogen bonding among water molecules, thereby enhancing water flux during MD.

Results

Toluene-induced phase transition of ZIF-8

We adjusted the synthesis conditions to produce different ZIF-8 variants: ZIF-8-1 was synthesized statically in methanol with $Zn(NO_3)_2$ for 24 h, while ZIF-8-2 involved a stirred synthesis with a different $Zn(NO_3)_2$ to 2-mlm ratio and mixing conditions (for full details, see the Methods section). ZIF-8-3 was synthesized via a 24-h static reaction in water using $Zn(OAc)_2$. These processes yielded rhombic dodecahedral ZIF-8 particles of differing sizes: 50 nm (ZIF-8-1), 410 nm (ZIF-8-2), and 2.5 μm (ZIF-8-3) (Supplementary Fig. 1). Their powder X-ray diffraction (PXRD) patterns (Supplementary Fig. 2a) are similar to the simulated pattern of ZIF-8 structure with sodalite topology. GSAS-II Rietveld refinement[46] (Fig. 1a and Supplementary Fig. 2b, c) on their PXRD patterns revealed that the three ZIF-8 samples comprised a mixture of cubic *I*-43*m*, monoclinic *Cm*, and triclinic *R*3*m* phases in varying proportions (ZIF-8-1: *I*-43*m*, 37.41%; *Cm*, 27.51%; *R*3*m*, 35.08%. ZIF-8-2: *I*-43*m*, 26.44%; *Cm*, 43.49%; *R*3*m*, 30.07%. ZIF-8-3: *I*-43*m*, 0%; *Cm*, 56.93%; *R*3*m*, 43.07%). The nitrogen sorption isotherms of the three ZIF-8 variants displayed type I curves and similar pore size distributions centered at 0.93 nm and BET surface areas around 1750 $m^2 g^{-1}$ (Supplementary Fig. 3). In addition, water vapor sorption profiles indicated that the obtained ZIF-8 variants exhibited hydrophobic pore environments with low water vapor adsorption ability (Supplementary Fig. 4).

We further analyzed their hydrothermal stability by immersing them in water at 70 °C for 10 days to ensure their integrity during MD processes. For ZIF-8-1, there was a noticeable decrease in crystallinity, with a specific surface area reduced to 85 $m^2 g^{-1}$, and inductively coupled plasma (ICP) analysis revealed partial Zn^{2+} leakage (Supplementary Fig. 5). PXRD and SEM analyses revealed distinct diffraction peaks corresponding to the (100), (002), (101), and (102) planes of ZnO and pronounced morphological changes (Supplementary Fig. 6). In contrast, the crystal structure, morphology and specific surface area of ZIF-8-2 and ZIF-8-3 remained unaltered, with negligible Zn^{2+} leakage (Supplementary Tables 1 and 2). Compared with ZIF-8-2 and ZIF-8-3, ZIF-8-1 exhibited a significantly lower N/Zn ratio (3.67) than the theoretical value of 4, as revealed by elemental analysis and ICP measurements, indicating a higher density of coordination defects (Supplementary Table 3). In addition, its smaller particle size (~50 nm) leads to an increased surface area-to-volume ratio, further contributing to the formation of surface defects. These defects facilitate the competitive coordination of water molecules with Zn^{2+} and protonation of terminal 2-methylimidazole ligands, weakening Zn–N bonds. As a result, Zn^{2+} is released from the framework, and the supernatant pH increases from 7.4 to 8.9 over 10 days. Meanwhile, Zn^{2+} reacts with OH^- to form ZnO precipitates[49,50].

Interestingly, despite the similar pore size distributions and nitrogen adsorption properties of the three ZIF-8 variants, their toluene adsorption behaviors exhibited distinct differences. The toluene adsorption curve of ZIF-8-1 at 25 °C indicates that it can rapidly adsorb toluene in the low-pressure region, followed by capillary condensation; during the desorption process, the condensed toluene is relatively easily desorbed (Fig. 1b). Like active carbon (Supplementary Fig. 7), when the temperature is raised to 60 °C, the toluene adsorbed in the low-pressure region is also removed upon pressure reduction. In contrast, ZIF-8-2's toluene adsorption and desorption at 25 °C showed multi-step adsorption behavior, with the adsorption amount increasing, reaching a plateau, and then increasing again to reach another plateau as pressure increased. Moreover, the toluene adsorbed does not desorb as pressure decreases. After increasing the temperature to 60 °C, the steps on the adsorption curve disappear, transitioning to rapid adsorption in the low-pressure region, and the amount of toluene adsorbed at 60 °C is slightly higher than at 25 °C (Fig. 1c). Unlike ZIF-8-1, the toluene adsorbed does not desorb upon reducing pressure, which is advantageous for capturing low-concentration toluene at high temperatures during the MD process. For ZIF-8-3, at both 25 °C and 60 °C, there were observable steps in adsorption, with difficult desorption, but the amount of toluene adsorbed, especially at lower partial pressures, was lower than the other two ZIF-8 variants.

The compositional changes in the different phases of ZIF-8 after toluene reached adsorption saturation at 60 °C were analyzed, which indicated all three ZIF-8 variants exhibited an increased proportion of the *Cm* phase (Fig. 1d). Specifically, for ZIF-8-1, portions of the *I*-43*m* and *R*3*m* phases transitioned to the *Cm* phase. In ZIF-8-2, the entire *I*-43*m* phase was converted to *Cm*, while in ZIF-8-3, only a part of the *R*3*m* phase underwent the transition to *Cm* (Supplementary Fig. 8). Notably, these phase transformations were reversible upon desorbing toluene under vacuum at 120 °C (Supplementary Fig. 9).

https://doi.org/10.1038/s41467-025-63267-8

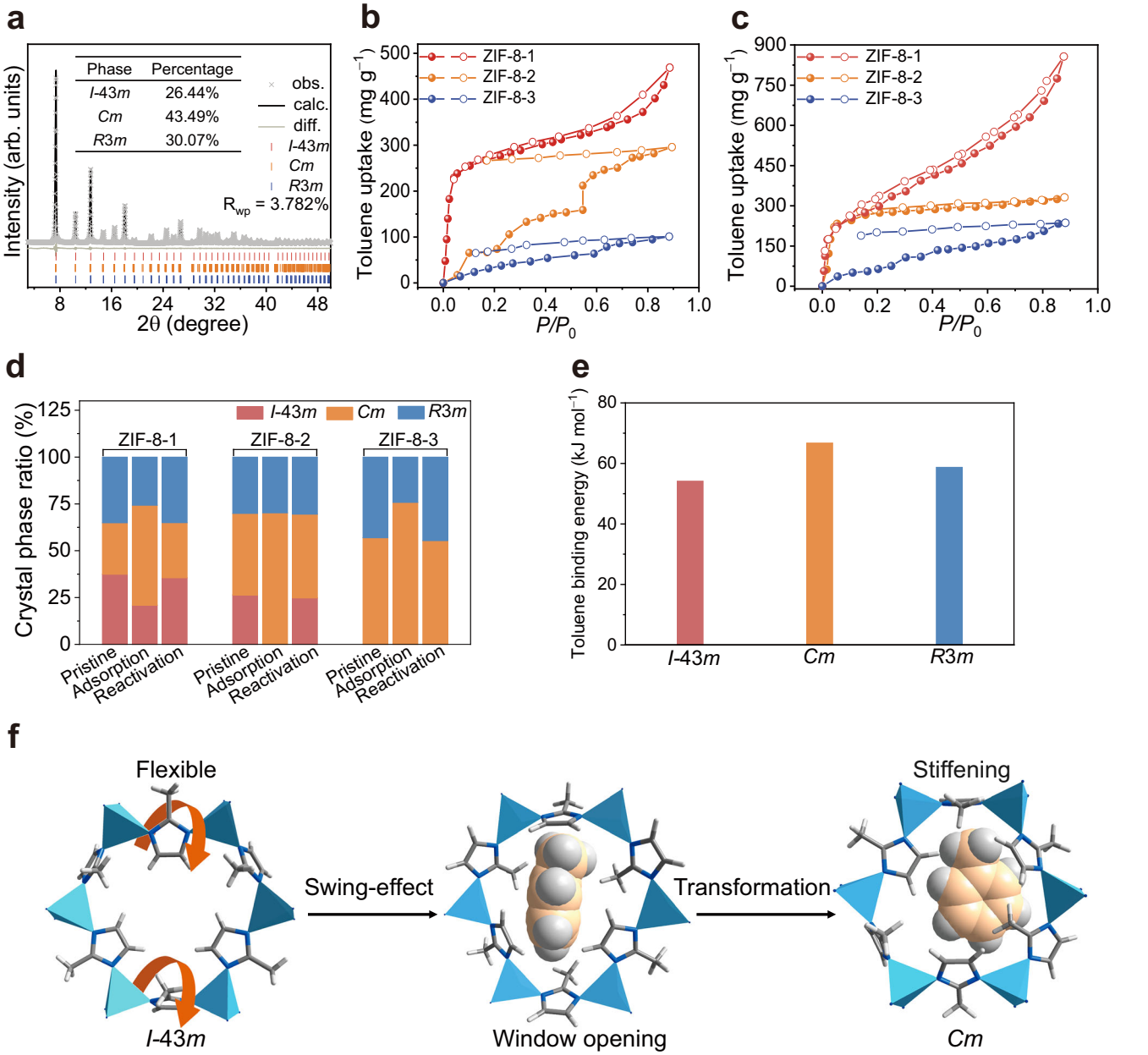

Fig. 1 | Toluene-induced crystal phase transition in various ZIF-8 variants. **a** PXRD Rietveld refinement results of primitive ZIF-8-2. The inset presents the relative phase composition ratios of the three crystalline phases. **b** Toluene vapor sorption of ZIF-8-1, ZIF-8-2, and ZIF-8-3 at 25 °C. **c** Toluene vapor sorption of ZIF-8-1, ZIF-8-2, and ZIF-8-3 at 60 °C. **d** Crystal phase composition ratios of pristine, toluene-saturated, and reactivated states of ZIF-8-1, ZIF-8-2, and ZIF-8-3 determined by PXRD Rietveld refinement. **e** Binding energies of toluene in three crystal phases of ZIF-8 using periodic DFT calculations. **f** Schematic diagram of toluene-induced transformation of ZIF-8 from the *I*-43*m* phase to the *Cm* phase, where the *Cm* phase exhibits greater stiffness compared to *I*-43*m*.

Further assessments of the host-guest interactions between toluene and ZIF-8 across different crystal phase were conducted through density functional theory (DFT) calculations (Supplementary Method 1 and Supplementary Data 1–3)[51,52]. In the *I*-43*m*, *Cm*, and *R*3*m* phases, the C-H···π distances between the toluene molecules and the 2-methylimidazole rings were measured at 3.251, 3.072, and 3.596 Å, respectively (Supplementary Fig. 10), correlating to toluene binding energies of 54.15, 66.73, and 58.71 kJ mol^{-1} (Fig. 1e). Toluene molecules entered the cavities in the *I*-43*m* phase through dynamic window and induced the transition to the *Cm* phase—a process verified through periodic DFT calculations (Fig. 1f and Supplementary Figs. 11–13). The *Cm* phase, characterized by a higher bulk modulus and a stiffer framework compared to the *I*-43*m* phase[46], was further reinforced by toluene molecules, effectively preventing their escape. In comparison, the absence of the *I*-43*m* phase in ZIF-8-3 made toluene adsorption more challenging. This distinct property of phase transition positions ZIF-8-2 as an exemplary candidate for toluene capture in MD processes.

Fabrication and characterization of ZIF-8 PE MMM-FDTS

We recently developed the TIPS-HoP method[48], capitalizing on its rapid film formation, scalability, and ability to produce MMMs with ultra-high MOF loadings (Fig. 2a). By adjusting the ratio of high-density polyethylene (HDPE) and ultra-high molecular weight polyethylene (UHMWPE) to ZIF-8, along with paraffin oil content, we fabricated self-supported ZIF-8 PE MMMs with ZIF-8-2 loadings ranging from 66% to 92%. PXRD and Fourier-transform infrared attenuated total reflectance (FTIR-ATR) confirmed the membranes' high crystalline and structural

https://doi.org/10.1038/s41467-025-63267-8

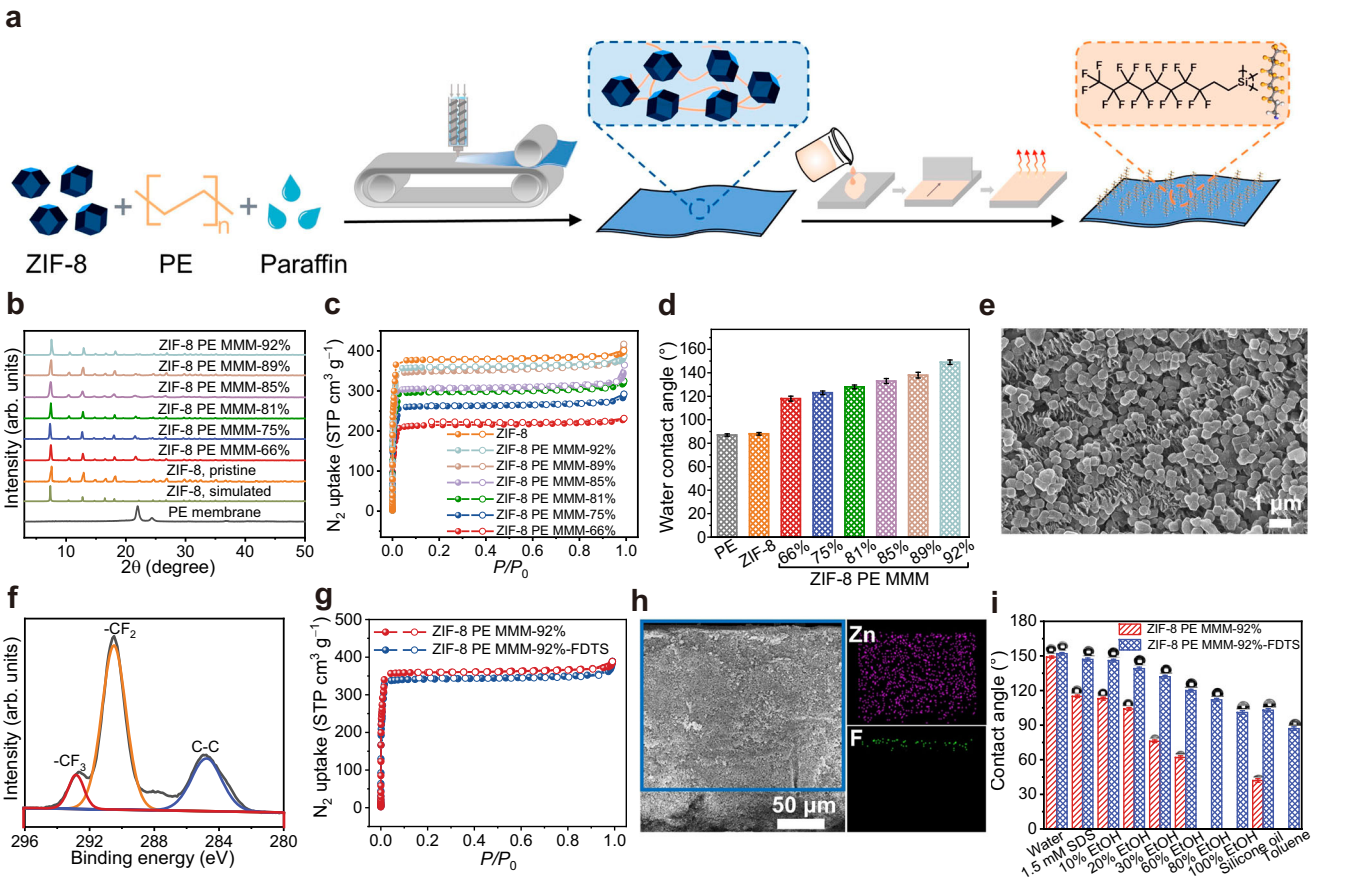

Fig. 2 | Preparation procedures and structural characterizations of ZIF-8 PE MMM-92%-FDTS. a Schematic diagram of the preparation process for ZIF-8 PE MMM-92%-FDTS. **b** PXRD spectra and **c** N_2 sorption curves of ZIF-8 PE MMMs with varying loadings. **d** Water contact angles with error bars representing the standard deviation of three independent samples; centers indicate mean values. **e** SEM image of corresponding ZIF-8 PE MMM-92% (scale bar, 1 μm). **f** High-resolution *C1s* XPS spectra ZIF-8 PE MMM-92%-FDTS. **g** N_2 sorption curves of ZIF-8 PE MMM-92% before and after fluorination. **h** Cross-section SEM image of the ZIF-8 PE MMM-92%-FDTS with corresponding spatial distribution of Zn and F (scale bar, 50 μm). **i** Contact angles of different liquids on ZIF-8 PE MMM-92% before and after fluorination; error bars represent standard deviation of three independent samples, centers indicate mean values.

integrity, while thermal gravimetric analysis verified the ZIF-8 loadings (Fig. 2b, Supplementary Figs. 14 and 15 and Supplementary Table 4). N_2 sorption isotherms demonstrated that increased ZIF-8 loading alleviated polymer-induced pore blockage, progressively enhancing the membrane's specific surface area from 965 to 1670 $m^2 g^{-1}$ for loadings from 66% to 92%, respectively (Fig. 2c, Supplementary Fig. 16 and Supplementary Table 5). Meanwhile, water contact angles rose from 118° to 149° (Fig. 2d, Supplementary Fig. 17 and Supplementary Table 6), augmenting the membranes' hydrophobicity and anti-wetting capabilities, a transformation attributable to a morphology shift from a polymer-dominant folded appearance to a multi-level rough structure jointly formed by the polymer and ZIF-8 (Fig. 2e and Supplementary Fig. 18)[53,54]. Additionally, mercury intrusion and nitrogen sorption analyses revealed that adding ZIF-8 introduced additional micropores, as evidenced by the pore size distribution peak around 0.9 nm, which was absent in the pure PE membrane. This significantly increases the cumulative pore volume below 2 nm. Additionally, mercury intrusion data indicated the formation of macropores around 448 nm due to ZIF incorporation (Supplementary Fig. 19).

To further improve the membrane's anti-fouling properties against oily contaminants, we coated their surface with 1H, 1H, 2H, 2H-perfluorodecyltrichlorosilane (FDTS), recognized for its low surface energy. Take ZIF-8 PE MMM-92%-FDTS as an example, FTIR-ATR analysis revealed distinct peaks for C-F stretching vibrations at 1211 cm^{-1}, and X-ray photoelectron spectroscopy (XPS) confirmed the presence of C-C, $-CF_2$, and $-CF_3$ groups, indicating successful fluorination (Fig. 2f and Supplementary Fig. 20a). This surface modification maintained the BET specific surface area at 1654 $m^2 g^{-1}$ (Fig. 2g and Supplementary Fig. 21). SEM and elemental mapping revealed fluorination preserved the original surface morphology, with fluorine primarily distributed in the upper membrane layer (Fig. 2h and Supplementary Fig. 20b). Post-fluorination, the oleophobicity of the membranes significantly increased, evidenced by the shift in ethanol and mineral oil contact angles from 0 and 42° to 101° and 103°, respectively (Fig. 2i and Supplementary Table 7). In contrast, fluorination of a relatively smooth commercial PVDF membrane only slightly improved its hydrophobicity, without significantly enhancing oleophobicity (Supplementary Fig. 22 and Supplementary Table 8), highlighting the distinct benefits offered by the micromorphology-induced FDTS arrangement in ZIF-8 PE MMMs[55,56]. The coated fluorides were firmly attached to the ZIF-8 PE MMM-92%-FDTS, as evidenced by the absence of leaching fluorides detected via liquid chromatography mass spectrometry after immersing the membrane in water at 70 °C for 5 days (Supplementary Table 9).

Membrane distillation performance

We evaluated the desalination efficacy of ZIF-8 PE MMMs using a cross-flow vacuum MD (VMD) setup, adjusting parameters such as temperature, absolute pressure, and NaCl solution feed concentration (Supplementary Fig. 23). For example, at a 10.5 wt% salt concentration, 70 °C temperature, and 85 kPa vacuum level, increasing ZIF-8 loading from 66% to 92% raised the ZIF-8 PE MMM flux from 7 to 68 L $m^{-2} h^{-1}$

https://doi.org/10.1038/s41467-025-63267-8

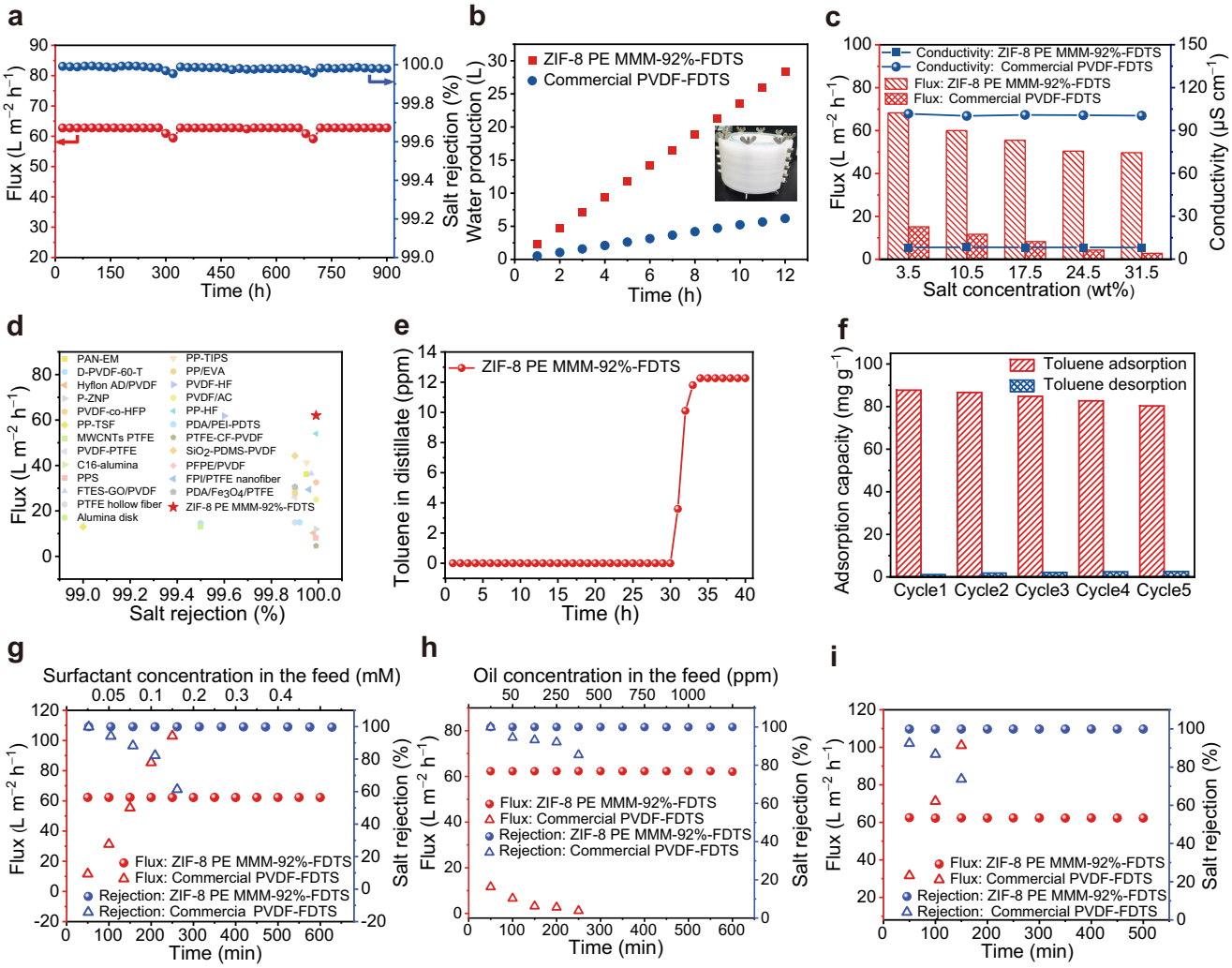

Fig. 3 | Desalination performance. a 900-h performance evaluation of ZIF-8 PE MMM-92%-FDTS at a feed temperature of 70 °C. **b** Membrane distillation test results of parallel stacked membrane modules (total effective membrane area: 452 cm^2), with a NaCl concentration of 10.5 wt%, feed-side temperature of 70 °C, and a vacuum level of 85 kPa. Inset shows a photograph of the parallel stacked membrane modules. **c** Influence of salt concentration on desalination performance of ZIF-8 PE MMM-92%-FDTS and commercial PVDF-FDTS membranes, at 70 °C feed temperature and 15 kPa absolute pressure. **d** Comparison of VMD performance (flux and rejection) between ZIF-8 PE MMM-92%-FDTS and literature reports. Corresponding data are provided in Supplementary Table 10. **e** Toluene concentration over time in the permeate at 200 ppm toluene feed concentration using ZIF-8 PE MMM-92%-FDTS membrane. **f** Toluene adsorption performance of ZIF-8 PE MMM-92%-FDTS evaluated over five cycles of VMD tests. **g** Water flux and salt rejection of ZIF-8 PE MMM-92%-FDTS and commercial PVDF-FDTS membranes with 10.5 wt% NaCl feed containing SDS (0.05–0.4 mM). **h** Water flux and salt rejection of the same membranes with 10.5 wt% NaCl feed containing mineral oil (50–1000 ppm). **i** Desalination performances comparison of ZIF-8 PE MMM-92%-FDTS and commercial PVDF-FDTS membranes with brines from power plants.

with the produced water's conductivity stable between 8 and 10 μS cm^{-1} (Supplementary Fig. 24a). By contrast, a commercial PVDF MD membrane, under identical conditions, exhibited a water flux of 23 L m^{-2} h^{-1} with a conductivity of 101 μS cm^{-1}. Post-fluorination, ZIF-8 PE MMM-92%-FDTS exhibited a sustained flux of 62 L m^{-2} h^{-1} with 99.99% salt rejection rate over a 100-h desalination process, significantly outperforming the PVDF-FDTS membrane which only managed a flux of 12 L m^{-2} h^{-1} before experiencing wetting after 10 h (Supplementary Fig. 24b). Moreover, a 900-h MD test on ZIF-8 PE MMM-92%-FDTS showed a stable water flux of 62 L m^{-2} h^{-1} for the first 300 h, which gradually decreased to 59 L m^{-2} h^{-1}. However, a simple backwash procedure effectively restored the flux while maintaining high salt rejection (Fig. 3a). Furthermore, SEM analysis after 900 h of operation revealed no significant surface scaling on the membrane (Supplementary Fig. 25), demonstrating its long-term anti-scaling capability. Increasing temperature or vacuum level enhanced the ZIF-8 PE MMM-92%-FDTS water flux, with the salt conductivity remaining less than 10 μS cm^{-1} (Supplementary Fig. 26). In a parallel stacked module with an effective membrane area of 452 cm^2, the membrane produced 28 L of pure water in 12 h, quintupling the output compared to a PVDF-FDTS membrane (Fig. 3b and Supplementary Fig. 27). Remarkably, at a salt concentration of 31.5 wt%, an optimal condition for reducing evaporative crystallization energy consumption towards zero liquid discharge, the ZIF-8 PE MMM-92%-FDTS still achieved a permeate flux of 50 L m^{-2} h^{-1}, whereas the fluorinated commercial PVDF-FDTS membrane's flux drastically reduced to 3 L m^{-2} h^{-1} (Fig. 3c). The ZIF-8 PE MMM-92%-FDTS membrane demonstrates a normalized flux of 71.8 L m^{-2} h^{-1} bar^{-1} by transmembrane pressure, ranking among the best reported for both polymeric and mixed matrix membranes in VMD (Fig. 3d, Supplementary Fig. 28 and Supplementary Table 10).

In practical applications such as shale gas wastewater treatment, typical VOC concentrations are around 10 ppm[57,58]. To accelerate the adsorption process and evaluate the upper performance of the membrane, we introduced 200 ppm toluene into a 10.5 wt% saline feed to test the VOC-trapping capability of the ZIF-8 PE MMM-92%-FDTS membrane. Remarkably, toluene remained undetectable (detection

limit: 2 ppb) in the permeate, far below the World Health Organization's warning limit of 0.7 ppm, until a breakthrough occurred after 30 h of continuous operation (Fig. 3e). The membrane exhibited a dynamic toluene adsorption capacity for toluene of 80 mg g^{-1} during the MD process. The saturated membrane (~16 mg toluene adsorbed in a 3 cm^2 area) was effectively regenerated by exposure to hot water vapor generated from 40 mL of water at 100 °C for 30 min, resulting in nearly complete desorption. It indicates that the membrane can be rapidly regenerated using low-grade heat sources, such as industrial waste heat, with toluene concentrations increasing from 10 ppm in the original feed to ~400 ppm in the collected condensate. This concentrated condensate can then be subjected to appropriate post-treatment methods[59–61]. The membrane maintained excellent performance after five-cycle tests (Fig. 3f). Additional testing with other common wastewater VOCs (ethylbenzene, chlorobenzene, p-xylene, aniline, and phenol each at 200 ppm) revealed maximum dynamic adsorption capacities of 63.9, 83.5, 59.6, 56.2, and 48.1 mg g^{-1}, respectively (Supplementary Fig. 29 and Supplementary Table 11). Based on a practical concentration of 10 ppm, our calculations indicate that the membrane can operate continuously for approximately 600 h before requiring regeneration, corresponding to the treatment of 38,000 L of wastewater per square meter of membrane area (Supplementary Table 12).

To evaluate the anti-wetting and anti-fouling properties of ZIF-8 PE MMM-92%-FDTS, we conducted VMD experiments using feed solutions with different concentrations of sodium dodecyl sulfate (SDS, an anionic surfactant) or mineral oil, under a 10.5 wt% salt concentration, 70 °C temperature, and 85 kPa vacuum[62,63]. In control tests using ZIF-8 PE MMM membranes without FDTS, we observed that the membranes without FDTS experienced wetting or fouling when exposed to surfactants or oil, which negatively impacted the MD performance (Supplementary Fig. 30). The introduction of 0.1 mM SDS led to an increased water vapor flux and decreased NaCl reduction to 82% for the commercial PVDF-FDTS membrane, indicating pore wetting (Fig. 3g). In contrast, ZIF-8 PE MMM-92%-FDTS retained its desalination efficiency even with 0.4 mM SDS, attributed to its omniphobic nature and a higher liquid entry pressure (0.28 MPa) versus 0.11 MPa for the PVDF-FDTS membrane. In anti-fouling tests, while the PVDF-FDTS membrane exhibited a significant decline in water flux with 250 ppm of mineral oil, the ZIF-8 PE MMM-92%-FDTS consistently maintained its performance, even when faced with 1000 ppm mineral oil, highlighting its superior fouling resistance (Fig. 3h). Subsequently, we tested the practical treatment capabilities of the ZIF-8 PE MMM-92%-FDTS membrane using power plant wastewater from Jinan, Shandong province and shale gas wastewater from Xuyong, Sichuan province, representative of complex compositions[64]. Throughout the testing, the performance of ZIF-8 PE MMM-92%-FDTS remained consistent, in contrast to the commercial PVDF-FDTS membrane, which underwent rapid wetting (Fig. 3i and Supplementary Fig. 31).

Evaporation enhancement mechanisms

To validate the impact of ZIF-8 with porous structure and swinging linkages on water evaporation, we prepared SiO_2 PE MMM-92%, as a control. It showed a BET surface area of 43 $m^2 g^{-1}$ and a rough surface morphology (Supplementary Fig. 32). Mercury intrusion and nitrogen adsorption analyses revealed that the total porosity of SiO_2 PE MMM-92% and ZIF-8 PE MMM-92% was comparable, yet ZIF-8 PE MMM-92% featured a significantly higher micropore volume (Supplementary Fig. 33 and Supplementary Table 13). VMD tests showed the flux of SiO_2 PE MMM-92% was only 28.7 L $m^{-2} h^{-1}$, significantly lower than that of ZIF-8 PE MMM-92% (Supplementary Fig. 34).

To elucidate the mechanism underlying the enhanced water flux observed in vacuum membrane distillation, molecular dynamics (MD) simulations were conducted (Supplementary Method 2)[65–67]. These simulations analyzed the evaporation of water molecules at the interface and quantified hydrogen bonds with 1000 water molecules placed above ZIF-8's crystal surface at 70 °C. We observed a significant increase in the rate of water molecule evaporation from the ZIF-8 with freely rotating imidazole linkages, marked by an increase in escaping water molecules and a decrease in hydrogen bond amount over 0–500 ps (Fig. 4a–c, Supplementary Fig. 35 and Supplementary Movie 1). In contrast, the calculated evaporation rate was negligible when the entire ZIF-8 structure was fixed. Moreover, MD simulations showed a much slower rate of water molecule evaporation on SiO_2's surface (Supplementary Figs. 36 and 37). These results illustrate that the oscillation of imidazole ligands within the hydrophobic micropores of ZIF-8 disrupts hydrogen bonding among water molecules, effectively accelerating water evaporation. Energy analysis further revealed that at 70 °C, ZIF-8 PE MMM reduced the evaporation and separation energy (ΔE) from 2316 J g^{-1} to 1955 J g^{-1} and the total energy per unit water produced (ΔE_{sys}) from 3928 J g^{-1} to 2895 J g^{-1}, compared to the SiO_2 PE MMM (Supplementary Method 3, Supplementary Figs. 38 and 39 and Supplementary Tables 14–19).

Discussion

Overall, we have uncovered mechanisms behind VOC-induced phase changes in ZIF-8, effectively trapping VOCs even under vacuum condition, and demonstrated a synergistic enhancement of water evaporation, driven by confined hydrophobic micropores and ligand oscillation. The developed omniphobic ZIF-8 PE MMM-92%-FDTS marks a significant advancement over traditional polymer membranes, offering superior VOC-trapping efficiency, higher water flux, and outstanding anti-fouling and anti-wetting properties. It enables the attainment of zero liquid discharge in settings where highly saline wastewater challenges reverse osmosis. Future research will focus on exploring various MOF structures to optimize VOC capture and enhance membrane durability in MD applications. Additionally, we aim to develop scalable manufacturing processes to achieve consistent batch preparation of ZIF-8 and continuous membrane fabrication.

Methods

Materials

All chemicals and solvents used in the syntheses were purchased from commercial suppliers and used without further purification. Zinc nitrate hexahydrate ($Zn(NO_3)_2{\cdot}6H_2O$, 98%) was purchased from Xilong Scientific Co., Ltd. Mineral oil was obtained from Oerlikon Co., Ltd. Ethanol (EtOH, AR), methanol (MeOH, AR), and CH_2Cl_2 (AR) were purchased from Beijing Tong Guang Fine Chemicals Company. High-density polyethylene (HDPE) and ultra-high molecular weight (UHMWPE) were procured from ALADDIN Chemical Co., Ltd. and Alfa Aesar (China) Chemical Co., Ltd. Paraffin was purchased from Fuchen (Tianjin) Chemical Reagent Co., Ltd. Sodium dodecyl sulfate (SDS, 98%) and 2-methylimidazole (2-mlm, 98%) were purchased from Shanghai Macklin Biochemical Co., Ltd. Toluene (AR) was purchased from Tianjin Fuyu Fine Chemical Co., Ltd. Ethylbenzene (98%) and 1H, 1H, 2H, 2H-Perfluorodecyltrichlorosilane (FDTS, 97%) were purchased from Meryer (Shanghai) Chemical Technology Co., Ltd. Chlorobenzene (99%), p-Xylene (98%), and sodium chloride (NaCl, 98%) were bought from Energy Chemical Co., Ltd. Commercial PVDF membranes were purchased from Merck Millipore. Deionized water (DI water) was produced by Milli-Q water purification system.

Synthesis of ZIF-8-1

$Zn(NO_3)_2{\cdot}6H_2O$ (1.4689 g, 4.94 mmol) was dissolved in 100 mL of methanol and added to a solution of 2-methylimidazole (1.6210 g, 19.74 mmol) in methanol (100 mL)[68]. The mixture was stirred well and left at room temperature for 24 h. Afterward, the solution was centrifuged, washed three times with methanol, and dried in a vacuum oven at 120 °C for 24 h to obtain ZIF-8-1 (ca. 0.85 g, 75%). Safety note: MeOH is flammable and toxic; $Zn(NO_3)_2{\cdot}6H_2O$ is an oxidizer and irritant.

https://doi.org/10.1038/s41467-025-63267-8

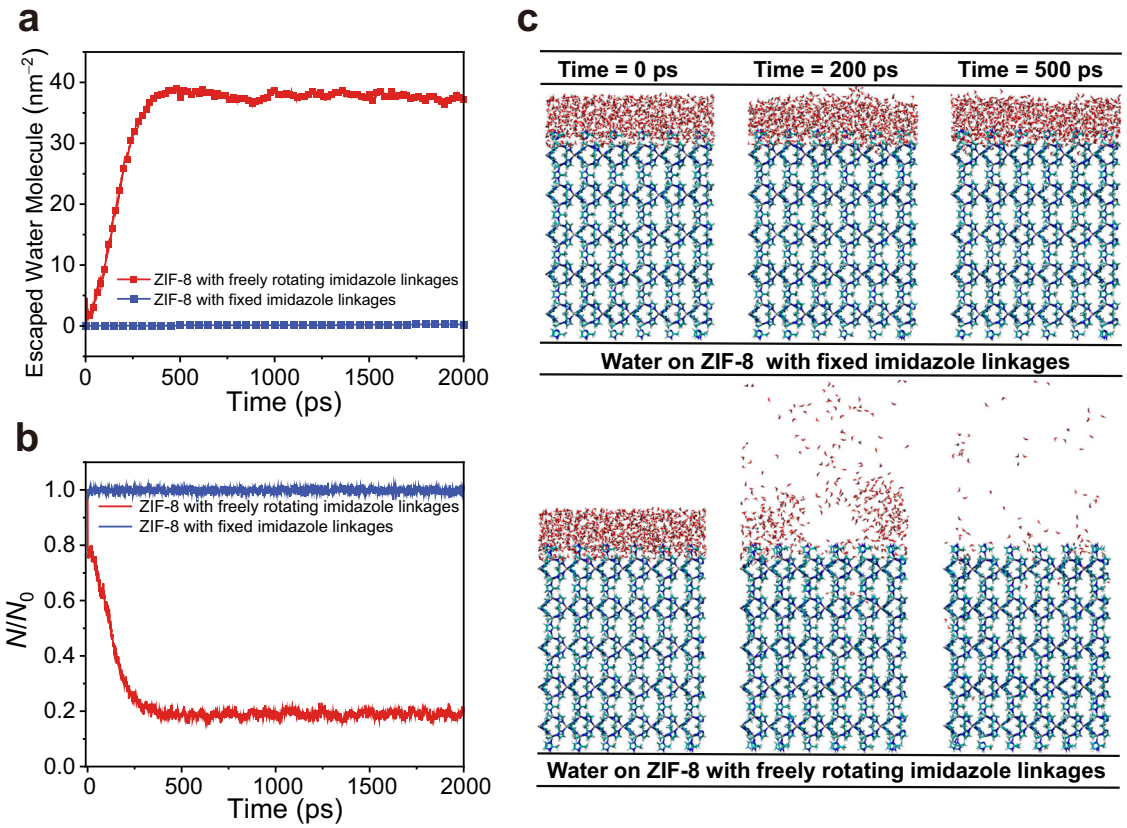

Fig. 4 | Evaporation enhancement mechanisms. a Number of water molecules escaping per square nanometer surface from ZIF-8 with fixed imidazole linkages and ZIF-8 with freely rotating imidazole linkages. **b** Ratio of the number of hydrogen bonds of 0–2000 ps water molecules on the surface of ZIF-8 with fixed imidazole linkages and ZIF-8 with freely rotating imidazole linkages (N) to the number of original hydrogen bonds (N_0). **c** Snapshots showing water evaporation on ZIF-8 with fixed and freely rotating imidazole linkages at 0, 200, and 500 ps.

Synthesis of ZIF-8-2

$Zn(NO_3)_2{\cdot}6H_2O$ (2.2517 g, 7.56 mmol) was dissolved in 50 mL of methanol, and 2-methylimidazole (2.6192 g, 31.9 mmol) was dissolved in 50 mL of methanol. The $Zn(NO_3)_2{\cdot}6H_2O$ methanol solution was then poured into the 2-methylimidazole methanol solution under stirring, and the mixture was stirred for 24 h at room temperature. Afterward, the mixture was centrifuged, washed three times with methanol, and dried in a vacuum oven at 120 °C for 24 h to obtain ZIF-8-2 (ca. 1.34 g, 78%). Safety note: MeOH is flammable and toxic; $Zn(NO_3)_2{\cdot}6H_2O$ is an oxidizer and irritant.

Synthesis of ZIF-8-3

$Zn(OAC)_2{\cdot}2H_2O$ (1.7560 g, 8.00 mmol) was dissolved in 20 mL of deionized water, and 2-methylimidazole (6.5680 g, 80.0 mmol) was dissolved in 100 mL of deionized water. The $Zn(OAC)_2{\cdot}2H_2O$ aqueous solution was then added dropwise into the stirred 2-mlm aqueous solution at 200 rpm, and the mixture stood for 24 h. Afterward, the mixture was centrifuged, washed once with water and twice with ethanol solutions, then dried in a vacuum oven at 120 °C for 24 h to obtain ZIF-8-3 (ca. 1.49 g, 82%). Safety note: $Zn(OAC)_2{\cdot}2H_2O$ is an irritant; 2-methylimidazole is harmful if inhaled.

Preparation of ZIF-8 PE MMM-wt%

A ZIF-8 PE MMM-92% was meticulously prepared by mixing pre-treated ZIF-8-2 (0.4600 g), HDPE (0.0321 g), and UHMWPE (0.008 g) with 0.3 mL of diluent paraffin. The mixture was stirred mechanically at 210 °C until it formed a viscous and homogeneous cast film material. Then, the cast film material was placed onto a conveyor belt operating at 40 rpm and subjected to roll-to-roll hot pressing at 120 °C. After cooling to ambient temperature, the membrane was immersed in 80 mL of CH_2Cl_2 overnight to remove the paraffin lubricant, followed by drying at ambient conditions.

Fabrication of omniphobic ZIF-8 PE MMM-92%-FDTS and commercial PVDF-FDTS membranes

Apply a 2 wt% FDTS n-hexane solution onto the surfaces of ZIF-8 PE MMM-92% or commercial PVDF membranes, then dry them in a vacuum oven at 120 °C for 2 h to obtain ZIF-8 PE MMM-92%-FDTS or commercial PVDF-FDTS.

Powder X-ray diffraction (PXRD)

PXRD patterns were collected using a Rigaku MiniFlex 600 instrument operating at 40 kV and 15 mA with monochromatic Cu-Kα radiation (λ = 1.54056 Å). Samples were mounted as whole thin films on a silicon zero-background holder. The PXRD patterns were recorded from 3 to 50° (2θ) with a step size of 0.02° and a scan rate of 2° per minute.

Field-emission scanning electron microscopy (FE-SEM)

Gold coating was performed using a Q150R ES coater, with a sputtering time of 120 s and a current of 23 mA. Prior to SEM imaging, the thin film samples were mounted on holders using conductive tape and coated with gold. SEM images were acquired using a ZEISS SUPRA-55 scanning electron microscope operating at 5 kV and 10 μA.

Fourier-transform infrared attenuated total reflection (FTIR-ATR)

FTIR-ATR spectra were recorded in the range of 400–4000 cm^{-1} on a Bruker ALPHA spectrometer with 24 scans.

Nitrogen sorption isotherm
Nitrogen adsorption isotherms were measured at 77 K using the Quantachrome instrument ASiQMVH002-5 analyzer to obtain surface area and pore size distribution. Before the testing, the samples were pre-treated at 120 °C under vacuum for 24 h to completely remove solvents from the pore channels. The pore size distribution was determined using the Non-Local Density Functional Theory (NLDFT).

Contact angle tests
The apparent contact angles of different liquids, including water, ethanol, toluene, and oil, on the membrane material were measured using the contact angle measurement instrument SCI3000 (Beijing Global EverTech Science and Technology Co., Ltd.). Three independent measurements were conducted with ~5 μL droplets of each liquid on each membrane.

Thermogravimetric analyses (TGA)
Thermal gravimetric analysis was performed using the DTG-60 instrument under a nitrogen atmosphere, with temperatures ranging from 40 to 800 °C and a flow rate of 50 mL min^{-1}. Prior to the test, all samples were dried in a vacuum oven at 120 °C.

Vapor adsorption isotherm measurements
The samples were analyzed for water vapor and organic sorption curves using the Belsorp Instrument Max analyzer. Prior to the tests, the samples were activated and pre-treated at 120 °C under vacuum for 12 h.

X-ray photoelectron spectroscopy (XPS)
The XPS spectra were obtained using the Thermo Scientific K-Alpha$^+$ XPS with a monochromatic Al Ka X-ray source (1486.6 eV) operating at 72 W (12 kV, 6 mA). Low-energy argon ion gun (≤10 eV) was used to neutralize the charge accumulation on the sample during the XPS experiment. Background subtraction was employed during XPS spectroscopy to eliminate baseline signals, and a mixed Gaussian-Lorentzian curve shape was used for spectrum fitting.

Thermal diffusivity tests
Thermal diffusivities were measured using a Laser Flash Apparatus (LFA, Netzsch LFA467) from 303 to 353 K.

Specific heat capacity (c_p) tests
Specific heat capacity tests were conducted on a differential scanning calorimetry (Netzsch DSC 204 F1) at a heating rate of 10 °C min^{-1} from 303 to 353 K under N_2 atmosphere.

Inductively coupled plasma-mass spectrometry (ICP-MS)
Zinc ion concentration in an aqueous solution of ZIF-8 immersion was determined using an inductively coupled plasma-mass spectrometry (ICP-MS, NexION 350, Perkin-Elmer, USA).

Headspace gas chromatography (HS-GC)
Headspace gas chromatography (Fuli HS930-GC9720Plus) was used to accurately determine the concentration of the benzene series.

Liquid chromatography mass spectrometry (LC-MS)
Liquid chromatography mass spectrometry (LC-MS) was measured using Thermo Scientific Ultimate 3000 UHPLC and Shimadzu LC-MS-2020.

Evaluation of MD performance
The MD performance of ZIF-8 PE MMM-92%-FDTS and commercial PVDF was evaluated in a vacuum MD configuration. The effective membrane area tested was 9 cm^2, with a feed volume of 1000 mL controlled at 70 °C and circulated to the membrane shell side at a flow rate of 4.957 g s^{-1}. The cavity side was maintained at around 15 mbar using a vacuum pump, and the vapor permeate on the cavity side was condensed by 5 °C water. The transmembrane water vapor flux J was determined by measuring the mass of the permeate. The conductivity of the permeate solution was monitored to evaluate the sodium chloride concentration. Each sample underwent three VMD trials, and average data were recorded.

Liquid entry pressure
The membrane was placed in a dead-end filtration setup, and the liquid entry pressure of the membrane was measured. Initially, 50 mL of deionized water was injected into the reservoir on the membrane and tightly sealed. Subsequently, compressed air was gradually pressurized (increased by 10 kPa each time, and stabilized for about 5 min). The pressure corresponding to the complete emergence of the first water drop was recorded as the liquid entry pressure. Three independent measurements were carried out for each membrane.

Statistical analysis and image processing
All graphs were plotted using Origin Pro 2021. Crystal structure illustrations were generated with Diamond 4.0.0. Schematic diagrams were created using Adobe Illustrator 2021. Phase compositions based on PXRD patterns were analyzed using GSAS-II. Particle size distributions from SEM images were analyzed using Nano Measurer 1.2.5.

Reporting summary
Further information on research design is available in the Nature Portfolio Reporting Summary linked to this article.

Data availability
The authors declare that the data supporting the findings of this study are available within the paper and its supplementary information files. Source data are provided with this paper.

References
1. Tong, T. & Elimelech, M. The global rise of zero liquid discharge for wastewater management: drivers, technologies, and future directions. *Environ. Sci. Technol.* **50**, 6846–6855 (2016).
2. Xie, W. et al. Charge-gradient hydrogels enable direct zero liquid discharge for hypersaline wastewater management. *Adv. Mater.* **33**, 2100141 (2021).
3. Kuang, X. et al. The changing nature of groundwater in the global water cycle. *Science* **383**, eadf0630 (2024).
4. Li, D., Yan, Y. & Wang, H. Recent advances in polymer and polymer composite membranes for reverse and forward osmosis processes. *Prog. Polym. Sci.* **61**, 104–155 (2016).
5. Tan, Z., Chen, S., Peng, X., Zhang, L. & Gao, C. Polyamide membranes with nanoscale turing structures for water purification. *Science* **360**, 518–521 (2018).
6. Drioli, E., Ali, A. & Macedonio, F. Membrane distillation: recent developments and perspectives. *Desalination* **356**, 56–84 (2015).
7. Jiang, M. et al. A bio-based nanofibre hydrogel filter for sustainable water purification. *Nat. Sustain.* **7**, 168–178 (2024).
8. Wang, Z. et al. Graphene oxide nanofiltration membranes for desalination under realistic conditions. *Nat. Sustain.* **4**, 402–408 (2021).
9. Chamani, H., Woloszyn, J., Matsuura, T., Rana, D. & Lan, C. Q. Pore wetting in membrane distillation: a comprehensive review. *Prog. Mater. Sci.* **122**, 100843 (2021).
10. Zuo, K. et al. Multifunctional nanocoated membranes for high-rate electrothermal desalination of hypersaline waters. *Nat. Nanotechnol.* **15**, 1025–1032 (2020).
11. Dudchenko, A. V., Chen, C., Cardenas, A., Rolf, J. & Jassby, D. Frequency-dependent stability of CNT Joule heaters in ionizable

media and desalination processes. *Nat. Nanotechnol.* **12**, 557–563 (2017).
12. Subrahmanya, T. M. et al. Self-surface heating membrane distillation for sustainable production of freshwater: a state of the art overview. *Prog. Mater. Sci.* **145**, 101309 (2024).
13. Deshmukh, A. et al. Membrane distillation at the water-energy nexus: limits, opportunities, and challenges. *Energy Environ. Sci.* **11**, 1177–1196 (2018).
14. Santoro, S., Avci, A. H., Politano, A. & Curcio, E. The advent of thermoplasmonic membrane distillation. *Chem. Soc. Rev.* **51**, 6087–6125 (2022).
15. Wang, M. et al. Ultrafast seawater desalination with covalent organic framework membranes. *Nat. Sustain.* **5**, 518–526 (2022).
16. Werber, J. R., Osuji, C. O. & Elimelech, M. Materials for next-generation desalination and water purification membranes. *Nat. Rev. Mater.* **1**, 16018 (2016).
17. Cho, W. et al. Supramolecular engineering of amorphous porous polymers for rapid adsorption of micropollutants and solar-powered volatile organic compounds management. *Adv. Mater.* **34**, 2206982 (2022).
18. Lou, M. et al. Difunctional MOF-wrapped graphene membranes for efficient photothermal membrane distillation and VOCs interception. *J. Membr. Sci.* **676**, 121592 (2023).
19. Ning, R. et al. Photocatalytic membrane for in situ enhanced removal of semi-volatile organic compounds in membrane distillation under visible light. *Sep. Purif. Technol.* **292**, 121068 (2022).
20. Lou, M., Zhu, X., Fang, X., Liu, Y. & Li, F. Interception of volatile organic compounds through CNT electrochemistry of electrified membrane surface during membrane distillation. *Sep. Purif. Technol.* **297**, 121380 (2022).
21. Kujawa, J., Al Gharabli, S., Kujawski, W. & Knozowska, K. Molecular grafting of fluorinated and nonfluorinated alkylsiloxanes on various ceramic membrane surfaces for the removal of volatile organic compounds applying vacuum membrane distillation. *ACS Appl. Mater. Interfaces* **9**, 6571–6590 (2017).
22. Boo, C., Lee, J. & Elimelech, M. Omniphobic polyvinylidene fluoride (PVDF) membrane for desalination of shale gas produced water by membrane distillation. *Environ. Sci. Technol.* **50**, 12275–12282 (2016).
23. Huang, Z., Yang, G., Zhang, J., Gray, S. & Xie, Z. Dual-layer membranes with a thin film hydrophilic MOF/PVA nanocomposite for enhanced antiwetting property in membrane distillation. *Desalination* **518**, 115268 (2021).
24. Wu, X. et al. Omniphobic surface modification of electrospun nanofiber membrane via vapor deposition for enhanced anti-wetting property in membrane distillation. *J. Membr. Sci.* **606**, 118075 (2020).
25. Wang, W. et al. Trade-off in membrane distillation with monolithic omniphobic membranes. *Nat. Commun.* **10**, 3220 (2019).
26. Zhang, N. et al. Janus membrane with hydrogel-like coating for robust fouling and wetting resistance in membrane distillation. *ACS Appl. Mater. Interfaces* **15**, 19504–19513 (2023).
27. Zhao, S. et al. Hydrophilicity gradient in covalent organic frameworks for membrane distillation. *Nat. Mater.* **20**, 1551–1558 (2021).
28. Abdollahzadeh, M. et al. Designing angstrom-scale asymmetric MOF-on-MOF cavities for high monovalent ion selectivity. *Adv. Mater.* **34**, 2107878 (2022).
29. Datta, S. J. et al. Rational design of mixed-matrix metal-organic framework membranes for molecular separations. *Science* **376**, 1080–1087 (2022).
30. Qian, Q. et al. MOF-based membranes for gas separations. *Chem. Rev.* **120**, 8161–8266 (2020).
31. Chen, G. et al. Solid-solvent processing of ultrathin, highly loaded mixed-matrix membrane for gas separation. *Science* **381**, 1350–1356 (2023).
32. Yadav, A., Yadav, P., Labhasetwar, P. K. & Shahi, V. K. CNT functionalized ZIF-8 impregnated poly(vinylidene fluoride-co-hexafluoropropylene) mixed matrix membranes for antibiotics removal from pharmaceutical industry wastewater by vacuum membrane distillation. *J. Environ. Chem. Eng.* **9**, 106560 (2021).
33. Gajipara, D. H., Kalla, S. & Murthy, Z. V. P. Desalination performance evaluation of hBN@UiO-66 MOF incorporated hollow fiber membrane using membrane distillation. *ChemistrySelect* **9**, e202402088 (2024).
34. Yang, F., Efome, J. E., Rana, D., Matsuura, T. & Lan, C. Metal–organic frameworks supported on nanofiber for desalination by direct contact membrane distillation. *ACS Appl. Mater. Interfaces* **10**, 11251–11260 (2018).
35. Furukawa, H., Cordova, K. E., O'Keeffe, M. & Yaghi, O. M. The chemistry and applications of metal-organic frameworks. *Science* **341**, 1230444 (2013).
36. Lai, C. et al. Metal-organic frameworks as burgeoning materials for the capture and sensing of indoor VOCs and radon gases. *Coord. Chem. Rev.* **427**, 213565 (2021).
37. Liu, G. et al. Eliminating lattice defects in metal–organic framework molecular-sieving membranes. *Nat. Mater.* **22**, 769–776 (2023).
38. Kitao, T., Zhang, Y., Kitagawa, S., Wang, B. & Uemura, T. Hybridization of MOFs and polymers. *Chem. Soc. Rev.* **46**, 3108–3133 (2017).
39. Li, J., Bhatt, P. M., Li, J., Eddaoudi, M. & Liu, Y. Recent progress on microfine design of metal–organic frameworks: structure regulation and gas sorption and separation. *Adv. Mater.* **32**, 2002563 (2020).
40. Zhou, S. et al. Asymmetric pore windows in MOF membranes for natural gas valorization. *Nature* **606**, 706–712 (2022).
41. Park, K. S. et al. Exceptional chemical and thermal stability of zeolitic imidazolate frameworks. *Proc. Natl. Acad. Sci. USA* **103**, 10186–10191 (2006).
42. Hobday, C. L. et al. Understanding the adsorption process in ZIF-8 using high pressure crystallography and computational modelling. *Nat. Commun.* **9**, 1429 (2018).
43. Wei, R. et al. Carbon nanotube supported oriented metal organic framework membrane for effective ethylene/ethane separation. *Sci. Adv.* **8**, eabm6741 (2022).
44. Yao, J. & Wang, H. Zeolitic imidazolate framework composite membranes and thin films: synthesis and applications. *Chem. Soc. Rev.* **43**, 4470–4493 (2014).
45. Zhou, S. et al. Paralyzed membrane: current-driven synthesis of a metal-organic framework with sharpened propene/propane separation. *Sci. Adv.* **4**, eaau1393 (2018).
46. Knebel, A. et al. Defibrillation of soft porous metal-organic frameworks with electric fields. *Science* **358**, 347–351 (2017).
47. Han, J. et al. Tuning the phase composition of metal–organic framework membranes for Helium separation through incorporation of fullerenes. *J. Am. Chem. Soc.* **145**, 14793–14801 (2023).
48. Wang, H. et al. Membrane adsorbers with ultrahigh metal-organic framework loading for high flux separations. *Nat. Commun.* **10**, 4204 (2019).
49. Liu, X. et al. Improvement of hydrothermal stability of zeolitic imidazolate frameworks. *Chem. Commun.* **49**, 9140–9142 (2013).
50. Zhang, H., Liu, D., Yao, Y., Zhang, B. & Lin, Y. S. Stability of ZIF-8 membranes and crystalline powders in water at room temperature. *J. Membr. Sci.* **485**, 103–111 (2015).
51. Huang, X. et al. Molecular exclusion separation of 1-butene isomers by a robust metal–organic framework under humid conditions. *Angew. Chem. Int. Ed.* **62**, e202303671 (2023).
52. Jiang, S. et al. Metal-organic frameworks for breakthrough separation of 2-butene isomers with high dynamic selectivity and capacity. *Angew. Chem. Int. Ed.* **62**, e202302036 (2023).
53. Nishimura, R. et al. Fractal surfaces of molecular crystals mimicking lotus leaf with phototunable double roughness structures. *J. Am. Chem. Soc.* **138**, 10299–10303 (2016).

54. Li, X. M., Reinhoudt, D. & Cregocalama, M. What do we need for a superhydrophobic surface? A review on the recent progress in the preparation of superhydrophobic surfaces. *Chem. Soc. Rev.* **36**, 1350–1368 (2007).
55. Zhang, W., Wang, D., Sun, Z., Song, J. & Deng, X. Robust superhydrophobicity: mechanisms and strategies. *Chem. Soc. Rev.* **50**, 4031–4061 (2021).
56. Su, B., Tian, Y. & Jiang, L. Bioinspired interfaces with superwettability: from materials to chemistry. *J. Am. Chem. Soc.* **138**, 1727–1748 (2016).
57. Tao, Z., Liu, C., He, Q., Chang, H. & Ma, J. Detection and treatment of organic matters in hydraulic fracturing wastewater from shale gas extraction: a critical review. *Sci. Total Environ.* **824**, 153887 (2022).
58. Vidic, R. D., Brantley, S. L., Vandenbossche, J. M., Yoxtheimer, D. & Abad, J. D. Impact of shale gas development on regional water quality. *Science* **340**, 1235009 (2013).
59. Barac, T. et al. Engineered endophytic bacteria improve phytoremediation of water-soluble, volatile, organic pollutants. *Nat. Biotechnol.* **22**, 583–588 (2004).
60. Yang, C. et al. Simultaneous removal of multicomponent VOCs in biofilters. *Trends Biotechnol.* **36**, 673–685 (2018).
61. Liu, G. et al. UV/H2O2: an efficient aqueous advanced oxidation process for VOCs removal. *Chem. Eng. J.* **324**, 44–50 (2017).
62. Wang, Y., Han, M., Liu, L., Yao, J. & Han, L. Beneficial CNT intermediate layer for membrane fluorination toward robust superhydrophobicity and wetting resistance in membrane distillation. *ACS Appl. Mater. Interfaces* **12**, 20942–20954 (2020).
63. Lu, K., Zuo, J., Chang, J., Kuan, H. & Chung, T. Omniphobic hollow-fiber membranes for vacuum membrane distillation. *Environ. Sci. Technol.* **52**, 4472–4480 (2018).
64. Vengosh, A., Jackson, R. B., Warner, N., Darrah, T. H. & Kondash, A. A critical review of the risks to water resources from unconventional shale gas development and hydraulic fracturing in the United States. *Environ. Sci. Technol.* **48**, 8334–8348 (2014).
65. Liu, Z. et al. Hierarchical photothermal fabrics with low evaporation enthalpy as heliotropic evaporators for efficient, continuous, salt-free desalination. *ACS Nano* **15**, 13007–13018 (2021).
66. Zhao, F. et al. Highly efficient solar vapour generation via hierarchically nanostructured gels. *Nat. Nanotechnol.* **13**, 489–495 (2018).
67. Wei, D. et al. Water activation in solar-powered vapor generation. *Adv. Mater.* **35**, 2212100 (2023).
68. Zhang, Y. et al. Preparation of nanofibrous metal–organic framework filters for efficient air pollution control. *J. Am. Chem. Soc.* **138**, 5785–5788 (2016).

Acknowledgements

This work was supported by the National Natural Science Foundation of China (nos. 22171022 (X.F.), 21971017 (B.W.), 21922502 (X.F.), and 22305016 (S.Z.)); Beijing Municipal Science and Technology Project (no. Z211100002421013 (B.W.)); China National Postdoctoral Program for Innovative Talents (no. BX20230464 (S.Z.)); China National Postdoctoral Science Foundation (no. 2023M730246 (S.Z.)); Beijing Institute of Technology Research Fund Program (no. 2022CX01003 (X.F.)). This research was supported by the Analysis and Testing Center of the Beijing Institute of Technology for basic characterization.

Author contributions

S.Z., X.F., and B.W. conceived and supervised the project. D.F.S. and X.L.L. carried out the synthesis, characterization of ZIF-8 PE MMMs, and membrane distillation tests. S.Z. participated in discussions related to membrane distillation testing. X.H., Y.H.Z., Z.P.W., and D.M. provided meaningful guidance on the ZIF-8 sorption discussion. C.S. assisted with toluene and water sorption isotherms experiments. Q.X.W. provided shale gas wastewater. D.F.S., X.F., and B.W. wrote and revised the manuscript. All authors discussed the results and assisted with manuscript preparation.

Competing interests

The authors declare no competing interests.

Additional information

Supplementary information The online version contains supplementary material available at https://doi.org/10.1038/s41467-025-63267-8.

Correspondence and requests for materials should be addressed to Xiao Feng, Shuang Zhao or Bo Wang.

Peer review information *Nature Communications* thanks the anonymous reviewers for their contribution to the peer review of this work. A peer review file is available.